Fatigue strength of blunt V-notched specimens produced by Selective Laser Melting of Ti-6Al-4V

S.M.J. Razavi[1*], P. Ferro[2], F. Berto[1], J. Torgersen[1]

[1] *Department of Mechanical and Industrial Engineering, Norwegian University of Science and Technology (NTNU), Richard Birkelands vei 2b, 7491, Trondheim, Norway*
[2] *Department of Engineering and Management, University of Padova, Stradella San Nicola 3, 36100 Vicenza, Italy*

Abstract

Selective Laser Melting (SLM) process is an Additive Manufacturing (AM) technique that allows producing metallic parts of any kind of geometry with densities greater than 99.5%. Complex shapes lead however to notches with different radii of curvature that may reduce load bearing capacities. This work is aimed to assess the fatigue strength of Ti-6Al-4V blunt V-notched samples produced by SLM. Results were compared with those of the corresponding smooth samples and Environmental Scanning Electron Microscopy (ESEM) have been used to investigate the fracture surface of the broken samples in order to identify crack initiation points and fracture mechanisms. Finally, the strain energy density approach was used to evaluate the critical radius value. Despite the observed fatigue strength reduction induced by the notch, samples showed a sufficient low notch sensitivity that it was not possible to define a critical radius for the material analysed.

Keywords: Additive Manufacturing, Blunt V-notch, Fatigue, Strain Energy Density, Titanium Alloy

Nomenclature

E	elastic modulus
f_{ij}, g_{ij}	eigenfunction
K_f	fatigue notch factor

* Corresponding author: S.M.J. Razavi
E-mail: javad.razavi@ntnu.no

K_I	notch stress intensity factor
K_t	stress concentration
q	notch sensitivity
R	loading ratio
R_c	critical radius
r_0	distance evaluated on the notch bisector line between the V-notch tip and the origin of the local coordinate system
T_σ	scatter band
$\bar{W}$	mean strain energy density
W_c	critical strain energy density
r, θ	polar coordinate parameters
α	half of notch opening angle
$\Delta\sigma$	loading range
$\Delta\sigma_A^{smooth}$	fatigue strength of smooth sample
$\Delta\sigma_A^{V-notch}$	fatigue strength of V-notched sample
σ_{ij}	stress components around the notch root
σ_{tip}	elastic maximum notch stress at notch root
λ_1, μ_1	eigenvalue
ρ	notch tip radius
Ω	critical volume
2D	two dimensional
3D	three dimensional
AM	additive manufacturing
BCC	body central cubic
CC	cubic crystal

ESEM	environmental scanning electron microscopy
FCC	face central cubic
HCF	high cycle fatigue
HCP	hexagonal close packed
HIP	hot isostatic pressing
OM	optical microscope
PBF-L	powder bed fusion-laser
PSB	persistent slip bands
SED	strain energy density
SLM	selective laser melting

1. Introduction

Additive manufacturing (AM) is a process that allows a part to be built layer-by-layer by using a combination of energy delivery and material deposition. Metallic parts are fabricated starting from powders that are melted by a laser or electron beam source. This results in a high sensitivity of material properties to process parameters. According to source parameters, the material can experience different thermal histories and thus different microstructures. The microstructure of AM parts can be highly anisotropic and can reach a density greater than 99.5% [1,2]. For example, columnar grains are shown to grow epitaxially through the deposition layers due to cooling [1]. Compared to traditional shaping processes, AM offers different advantages such as a faster time-to market, a near-net-shape production without the need of expensive moulds and tools, a high efficiency in material utilization, the possibility to directly fabricate geometries based on CAD models and a high level of flexibility. On the other hand, AM parts suffer the presence of defects often related to non-optimal scan parameters such as unmolten particles, spherical entrapped gas bubbles, and lack of fusion [3]. Among the AM processes, a particular attention is paid on SLM, a Powder Bed Fusion-Laser (PBF-L) method [4,5]. The possibility to create geometrically complex

structures of high performance materials has made SLM particularly interesting for aerospace and biomedical industry, where titanium alloys, and in particular Ti-6Al-4V, are widely used. Titanium alloys are in fact characterized by excellent corrosion resistance, high specific strength, low density and low elastic modulus.

Both in aerospace and biomedical applications, fatigue is the primary mechanism of rupture of components such as turbine blade, hip prosthesis and mechanical heart valve. For this reason, the fatigue strength of additive manufactured parts is highly studied in literature. In their work about high cycle fatigue behaviour of SLM-processed Ti-6Al-4V, Leuders et al. [6] found that porosity act as strong stress raisers and lead to failure. In order to improve the fatigue strength of titanium alloy TiAl6V4 manufactured by SLM, reduction of porosity was thus considered by authors much more important than microstructure optimization. In a more recent work [7], Kasperovich and Hausmann found a reduction in fatigue resistance of SLM processed TiAl6V4 compared to the wrought alloy due to a combination of the unfavourable martensitic microstructure, unmolten particles, pores, and microcracks. Finally, they found that in order to restoring the fatigue resistance of the conventionally processed TiAl6V4, SLM-processed samples need to be subjected to Hot Isostatic Pressing (HIP), which reduces porosity, and surface machining which reduces surface roughness. As a matter of fact, for components that cannot be machined on all surfaces, the rough 'as built' surface needs to be considered as crack initiator in the design process and their lower fatigue strength has to be taken into account. Finally, in that work, heat treatments were found not to give a significant improvement on High Cycle Fatigue (HCF) strength.

In orthopaedic implant or aerospace design, the presence of geometrical fillets such as notches which cause stress locally is unavoidable. It is necessary to pay attention to these notches, because they effect the fatigue resistance of component. Considering that the safety of structure is vital in air vehicles, especially in manned vehicles like the civil airplanes etc., it is necessary to strictly evaluate the resistance of the light alloys against crack initiation from the notch border, experimentally and/or theoretically [8-12].

Among the methods used for the fracture and fatigue stress assessment of notch components, the Strain Energy Density (SED) approach is one of the most used in recent literature. This method was firstly introduced by Lanzzarin and Zambardi in 2001 [13] and then deeply investigated by Lazzarin, Berto and co-workers [14-16]. The fatigue strength is evaluated in terms of strain energy density averaged over a control volume of radius R_c around the notch tip. The critical radius, R_c, is a material property. That criterion was successfully applied to assess the fatigue strength of welded structures [17] as well brittle and ductile fracture of cracked and notched specimens under mixed mode loading [18-21]. Finally, in recent years, the SED approach was used for the evaluation of thermal load-induced notch stress intensity factor [22,23] and the influence of residual stress on fatigue strength of welded joints [24-27]. Even if HCF tests on AM smooth samples were deeply investigated in literature, the fatigue strength assessment of AM notched samples is still open and worthy of investigation.

The present work is aimed at studying the fatigue behaviour of Ti-6Al-4V notched specimens obtained by SLM process; in addition to the critical radius evaluation, fatigue notch factor and notch sensitivity on the fatigue strength of analysed samples will be discussed.

2. Analytical background

An analytical approach for describing local stress field ahead of rounded V-notches was previously proposed by Filippi et al. [28]. The stress components were written by separating the contribution due to the symmetric solution (mode I) from that due to the skew-symmetric solution (mode II). With reference to the coordinate system shown in Fig. 1, mode I stresses are [28]:

$$\sigma_{ij} = a_1 r^{\lambda_1 - 1} \left[f_{ij}(\theta,\alpha) + \left(\frac{r}{r_0} \right)^{\mu_1 - \lambda_1} g_{ij}(\theta,\alpha) \right] \quad (1)$$

where $\lambda_1 > \mu_1$ and the parameter a_1 can be expressed either via the notch stress intensity factor K_1 in the case of a sharp, zero radius, V-notch or by means of the elastic maximum notch stress σ_{tip} in the case of blunt V-notches. In Eq. (1) r_0 is the distance evaluated on the notch bisector line between

the V-notch tip and the origin of the local coordinate system; r_0 depends both on the notch root radius ρ and the opening angle 2α (Fig. 1), according to the expression $r_0 = \rho[(\pi - 2\alpha)/(2\pi - 2\alpha)]$. The angular functions f_{ij} and g_{ij} are given in Ref. [28]:

$$\begin{Bmatrix} f_{\theta\theta} \\ f_{rr} \\ f_{r\theta} \end{Bmatrix} = \frac{1}{1+\lambda_1+\chi_{b_1}(1-\lambda_1)} \times \left[\begin{Bmatrix} (1-\lambda_1)\cos(1-\lambda_1)\theta \\ (3-\lambda_1)\cos(1-\lambda_1)\theta \\ (1-\lambda_1)\sin(1-\lambda_1)\theta \end{Bmatrix} + \chi_{b_1}(1-\lambda_1) \begin{Bmatrix} \cos(1+\lambda_1)\theta \\ -\cos(1+\lambda_1)\theta \\ \sin(1+\lambda_1)\theta \end{Bmatrix} \right] \tag{2}$$

$$\begin{Bmatrix} g_{\theta\theta} \\ g_{rr} \\ g_{r\theta} \end{Bmatrix} = \frac{1}{4(q-1)\left[1+\lambda_1+\chi_{b_1}(1-\lambda_1)\right]} \times \left[\begin{matrix} \chi_{d_1} \begin{Bmatrix} (1-\mu_1)\cos(1-\mu_1)\theta \\ (3-\mu_1)\cos(1-\mu_1)\theta \\ (1-\mu_1)\sin(1-\mu_1)\theta \end{Bmatrix} + \\ \chi_{c_1}(1-\lambda_1) \begin{Bmatrix} \cos(1+\mu_1)\theta \\ -\cos(1+\mu_1)\theta \\ \sin(1+\mu_1)\theta \end{Bmatrix} \end{matrix} \right] \tag{3}$$

The eigenfunctions f_{ij} depend only on Williams' eigenvalue, λ_1, which controls the sharp solution for zero notch radius. The eigenfunctions g_{ij} mainly depend on eigenvalue μ_1, but are not independent from λ_1. Since $\mu_1 < \lambda_1$, the contribution of μ-based terms in Eq. (3) rapidly decreases with the increase of the distance from the notch tip. All parameters in Eqs. (1–3) have closed form expressions but here, for the sake of brevity, only some values for the most common angles are reported in Table 1 [28]. Under plane-stress conditions $f_{zz}(\theta)=g_{zz}(\theta)=0$.

Fig. 1. Coordinate system and symbols used for the stress field components ($q = \frac{2\pi - 2\alpha}{\pi}$, $\rho = \frac{qr_o}{q-1}$).

Table 1. Parameters for the stress distribution [28].

The SED approach is based on the idea that under tensile stresses failure occurs when $\overline{W} = W_c$, where the critical value W_c varies from material to material. The same criterion can be extended to fatigue strength assessment where each nominal stress amplitude corresponds a critical value of the SED averaged over the control volume of radius R_c. Dealing with blunt notches, it is possible to

determine the total strain energy over the crescent shape volume and then the mean value of the SED, by using the elastic maximum notch stress. The mean value of SED can be expressed as a function of the stress at the notch tip, σ_{tip}. More precisely:

$$\bar{W}_1 = F(2\alpha) \times H(2\alpha, \frac{R_c}{\rho}) \times \frac{\sigma_{tip}^2}{E} \quad (4)$$

where $F(2\alpha)$ depends on the notch opening angle and H is a function of the notch opening angle, 2α, R_c/ρ ratio, and Poisson's ratio [15]. Fig. 2 shows the geometrical parameters that define the critical volume (area), Ω, for blunt V-notch under mode I loading condition. In addition to the analytical method (Eq. 4), finite element analysis can be conducted to obtain the mean SED values.

Fig. 2. Critical volume (area) for blunt V-notch under mode I loading condition.

3. Material, geometries and experimental procedure

The analysed Ti-6Al-4V samples were produced by means of SLM by using optimized process parameters that guaranteed a density greater than 99.7%. Numerous methods have been proposed by scholars for surface treatment of components made by AM. Application of high quality powder and optimum fabrication parameters commonly is reported to improve the final quality of the part [29-31]. However, several post‐process surface treatment techniques have also been used to improve the geometrical accuracy of the final parts [32]. Conventional surface preparation methods such as machining, mechanical polishing, abrasive flow polishing, chemical milling and electroplating have been considered for treating the surface of AM components [32]. In this research, after samples production by AM process, specimens were sandblasted at 6 bar using corundum sand with a mean grain size of 220 μm. They were then stress relief heat-treated in non-controlled atmosphere (heating rate: 10.8 °C/min; holding time: 3h at 650 °C; cooling rate: 2 °C/min) and after cutting off the base plate they were re-sandblasted at 6 bar using corundum sand. All specimens were obtained by using a layer thickness of 60 μm. Fig. 3 shows the geometries of

smooth and blunt V-notched specimens. The radius at the notch tip is 1 mm while the thickness of the samples is 3 mm.

Fig. 3. Geometries of smooth and blunt V-notched specimens and built axis (Z) (dimensions in mm).

For each geometry ten specimens were tested under axial fatigue loading. Fatigue tests were carried out by using a universal MTS machine (250 kN). All tests have been carried out under load control, using a sinusoidal signal in uniaxial tension with a frequency of 10 Hz and load ratio $R = 0$. The run out limit was set equal to 10^6 cycles. The microstructure and the fracture surface of the samples were investigated by Optical Microscope (OM) and environmental scanning electron microscope (ESEM) (FEI QUANTA 400), respectively.

Kroll's Reagent (2ml HF, 2 ml HNO_3, 100 ml H_2O) was used as metallographic etchant. The alpha prime and acicular alpha structures of titanium alloy will appear white after etching while intergranular beta structure and beta grains will be darkened.

A numerical model under plane-stress condition was carried out using Ansys® numerical code in order to calculate both the strain energy density averaged over the control volume of radius R_c and the stress concentration factor, K_t. Young modulus and Poisson's coefficient were set equal to 110 GPa and 0.34, respectively. The geometry was meshed using the mesh free option with an element (PLANE 183) dimension of 0.1 mm. Finally, a 3D model was also carried out to verify the goodness of the plane-stress condition hypothesis used in the 2D model.

4. Results

4.1 Fatigue test results

Results obtained from the statistical elaboration of fatigue tests data for smooth and notched samples are reported in Figs. 4 and 5, respectively. Values of stress amplitude related to a survival probability of 50%, the slope of the Wöhler curve and the scatter index T_σ (the ratio between the

stress amplitudes corresponding to 10% and 90% of survival probability) are reported in the above-cited figures. Specimens survived over 1 million cycles are considered as run out and marked up with an arrow. It can be noted that the difference between the Wöhler curves are related both to the mean value of the stress amplitude at 1×10^6 cycles, and to the scatter index T_σ. The fatigue strength of blunt V-notch specimen at 1 million cycles was 144 MPa compared to a value of 243 MPa related to the fatigue strength of smooth sample.

Fig. 4. Fatigue life of smooth samples.

Fig. 5. Fatigue life of double blunt V-nothced samples.

4.2 – Microstructure and fractography

A preliminary microstructure investigation by means of OM showed an almost porosity-free material. Some sporadic porosity was found which dimension was less than 50 μm. OM and ESEM micrographs are shown in Fig. 6. The grains appears acicular with a prevalence of α' plates surrounded by a little percentage of β phase. In Fig. 6a the primary equiassic morphology of β phase prior to the β → α' transformation can be also observed. In Fig. 6b, the Al-reach black zones correspond to α' phase, tempered by stress-relief heat treatment, while the white zones, reach in vanadium, correspond to β phase. Such a microstructure is due to the high cooling rate that characterizes the SLM process and the subsequent heat treatment below 800 °C.

Fig. 6. OM (a) and ESEM (b) micrographs of the sample in xy plane.

ESEM fractographs of the smooth and blunt double V-notched specimens are shown in Figs. 7 and 8, respectively.

Fig. 7. ESEM fractographs of the smooth specimen ($\Delta\sigma$ = 320 MPa, Cycles Number = 410225).

Fig. 8. ESEM fractographs of the double blunt V-notched specimen ($\Delta\sigma$ = 220 MPa, Cycles Number = 156035).

It is noted that fatigue cracks nucleate at the specimen surface both in smooth and double V-notched specimens where severe intrusions (see Fig. 8c), due to the roughness, act as crack initiation points (Figs. 7d and 8b). The fracture nucleates at one point at the surface of the smooth sample (Fig. 7d) and propagates towards the opposite edge covering almost the entire cross section of the sample until the final rupture. The final fracture surface, characterized by dimples (Fig. 7c), was found to be inclined by about 45° with respect to the load direction (Fig. 7a). No porosity was observed on fracture surface of all samples. In a similar way, fatigue cracks nucleate at both the notch tip of the double V-notched sample (Fig. 8). Thus, the final fracture surface appears in between the two propagation zones and still inclined by about 45° with respect to the load direction (Fig. 8a). Fig. 8b shows a typical deep intrusion where a crack nucleated.

4.3 – Critical Radius (R_c)

By referring to the fatigue strength of the smooth and double V-notched samples at 1 million cycles, the R_c value was obtained by equating the strain energy density of the smooth sample to the strain energy density averaged over the sector of radius R_c around the blunt V-notch of the double V-notched specimen according to the following equation (5):

$$\Delta \bar{W}_c^{\,smooth} = \frac{\left(\Delta\sigma_A^{smooth}\right)^2}{2E} = \Delta \bar{W}_c^{\,bluntV-notch}(R_c) \tag{5}$$

where $\Delta\sigma_A^{smooth}$ is the fatigue strength of the smooth sample at 10^6 cycles (243 MPa) and E is the Ti-6Al-4V elastic modulus (110000 MPa). Eq. (5) was calculated numerically by using the nominal fatigue strength of the double blunt V-notched sample at 10^6 cycles ($\Delta\sigma_A^{V\text{-}notch}$=144 MPa) and by varying the critical radius value until the strain energy density averaged over the sector of radius R_c

was equal to $\Delta\bar{W}_c^{smooth}$. The main features of the in-plane-stress distributions and the variations of the stress concentration factor as a function of the specimen thickness were studied in several researches [33-35]. According to these researches, the fracture modes are coupled in 3D analyses. Before starting with the parametrical analysis, a 3D model was carried out in order to verify the plane-stress hypothesis adopted in the 2D model. By using a value of R_c equal to 0.6 mm the SED obtained with the 3D model was found to be 1.025 MJ/m^3 against a value of 1.03 MJ/m^3 obtained with the 2D model under plane-stress condition. Fig. 9 shows the numerical value of $\Delta\bar{W}_c^{bluntV-notch}$ as a function of the critical radius (R_c) and the SED value corresponding to the smooth sample at 10^6 cycles. It is observed that a R_c value for the double blunt V-notched specimen cannot be defined since it would exceed the resistant section dimension (R_c > 5 mm).

Fig. 9. Numerical value of $\Delta\bar{W}_c^{bluntV-notch}$ as a function of the critical radius, R_c.

5 – Discussion

The impossibility to define a critical radius suggests a very low notch sensitivity of the analysed material. The notch sensitivity (q) is defined by equation (6):

$$q = \frac{K_f - 1}{K_t - 1} \tag{6}$$

where K_f is the fatigue notch factor ($K_f = \Delta\sigma_A^{smooth} / \Delta\sigma_A^{V-notch}$) and K_t is the stress concentration factor defined by maximum local stress to nominal stress ratio ($K_t = \sigma_{\max} / \sigma_{nom}$). The nominal stress is defined as the average stress across the reduced specimen cross-section in the presence of the notch. In general, $0 \le q \le 1$. When the theoretical stress concentration factor equals the fatigue notch factor (i.e. $K_f = K_t$), q = 1. If the notch has no adverse effect on the fatigue limit (i.e. K_f = 1), q = 0. By using the fatigue data obtained in this work, K_f = 1.69. K_t was found equal to 6.8 by a numerical simulation. This results in a q value equal to 0.12.

A low notch sensitivity of the wrought Ti-6Al-4V alloy was already observed by Hosseini [36]. He justified such alloy behaviour through alpha Hexagonal Close Packed (HCP) crystal lattice characteristics. Compared to cubic lattices, such as Face Central Cubic (FCC) or Body Central Cubic (BCC) lattice, the slip planes in HCP lattice are all parallel to each other (planes (0001) in Miller-Bravais system). The slip systems number for dislocations in a HCP lattice are thus very low if compared to those in a Cubic Crystal (CC). Now, dislocations play a major role in the fatigue crack initiation phase. It has been observed that after a large number of loading cycles dislocations pile up and form structures called Persistent Slip Bands (PSB). Such PSB can be formed more easily in a crystal grain that has an unfavourable orientation of its slip planes relative to the planes of maximum applied shear stresses (Fig. 10). Because of its few slip systems, for a HCP lattice, such unfavourable orientations are very few. In this situation, many potential damage initiation sites occur within the volume of a smooth specimen but, at the sharp notch, there is a possibility that no damage initiation site occurs in the small region where the stress is near its peak value. Hence, on the average, the notched member will be more resistant to fatigue if the comparison is made on the basis of the local notch stress.

Fig. 10. Schematic representation of PSB formed in a crystal grain that has an unfavourable orientation of its (0001) slip planes relative to the planes of maximum applied shear stresses.

In SLM-processed samples, fatigue cracks were observed to initiate on severe surface intrusions due to the high roughness induced by the process itself as shown in Fig. 11. Such intrusions are covered by an oxide layer which was formed during the stress-relief heat treatment and non-cleaned up by the grinding treatment. Now, the number of potential crack initiation intrusions is thought to be much higher in smooth samples than in the sharp V-notch specimen where there is the possibility that no such critical surface defects occur in the small region near the notch tip. This effect makes the notch sensitivity of the SLM-processed Ti-6Al-4V alloy very low as observed by experiments.

Fig. 11. Surface intrusions induced by the SLM process.

5. Conclusions

The fatigue strength of Ti-6Al-4V blunt V-notched samples produced by SLM was assessed. Results were compared with those corresponding to smooth samples and ESEM have been used to investigate the fracture surface of broken samples in order to identify crack initiation points and fracture mechanisms. Despite the fatigue specimens were weakened by the sharp V-notch, a low notch sensitivity was measured. This was attributed both to the hexagonal crystal lattice of tempered alpha prime grains and to the high roughness detected on sample surface. Finally, the strain energy density approach was used to evaluate the critical radius value. However, because of the low notch sensitivity which was found to characterize the material, it was observed that the radius of critical volume for blunt V-notched specimen cannot be defined since it would exceed the resistant section dimension of the tested samples.

References

[1] X. Wu, J. Liang, J. Mei, C. Mitchell, P.S. Goodwin, W. Voice, Microstructures of laser-deposited Ti-6Al-4V, Mater. Design 25(2) (2014) 137-144

[2] E. Wycisk, S. Siddique, D. Herzog, F. Walther, C. Emmelmann, Fatigue performance of laser additive manufactured Ti-6A-4V in very high cycle fatigue regime up to 10^9 cycles, Front. Mater. 2 (2015) (DOI: 10.3389/fmats.2015.00072).

[3] T. Vilaro, C. Colin, J.D. Bartout, As-fabricated and heat-treated microstructures of the Ti-6Al-4V alloy processed by selective laser melting, Metall. Mater. Trans. A 42A(10) (2011) 3190-3199.

[4] J.P. Kruth, P. Mercelis, J. Van Vaerenbergh, L. Froyen, M. Romboust, Binding mechanism in selective laser sintering and selective laser melting, Rapid Prototyping J. 11(1) (2005) 26-36

[5] B. Vrancken, L. Thijs, J.P. Kruth, J.V. Humbeeck, Heat treatment of T6Al4V produced by selective laser melting: microstructure and mechanical properties. J. Alloys Compd. 541(0) (2012) 177-185.

[6] S. Leuders, M. Thöne, A. Riemer, T. Niendorf, T. Tröster, H.A. Richard, H.J. Maier, On the mechanical behaviour of titanium alloy TiAl6V4 manufactured by selective laser melting: fatigue resistance and crack growth performance, Int. J. Fatigue 48 (2013) 300-307.

[7] G. Kasperovich, J. Hausmann, Improvement of fatigue resistance and ductility of Ti-6Al-4V processed by selective laser melting, J. Mater. Process. Technol. 220 (2015) 202-214.

[8] S.M.J. Razavi, M.R. Ayatollahi, C. Sommitsch, C. Moser, Retardation of fatigue crack growth in high strength steel S690 using a modified stop-hole technique, Eng. Fract. Mech. 169 (2017) 226–237.

[9] M.R. Ayatollahi, S.M.J. Razavi, C. Sommitsch, C. Moser, Fatigue life extension by crack repair using double stop-hole technique, Mater. Sci. Forum 879 (2017) 3-8.

[10] M. R. Ayatollahi, S.M.J. Razavi, M.Y. Yahya, Mixed mode fatigue crack initiation and growth in a CT specimen repaired by stop hole technique, Eng. Fract. Mech. 145 (2015) 115-127.

[11] M.R. Ayatollahi, S.M.J. Razavi, H.R. Chamani, A numerical study on the effect of symmetric crack flank holes on fatigue life extension of a SENT specimen, Fatigue Fract. Eng. Mater. Struct. 37(10) 1153-1164.

[12] M.R. Ayatollahi, S.M.J. Razavi, H.R. Chamani, Fatigue Life Extension by Crack Repair Using Stop-hole Technique under Pure Mode-I and Pure mode-II Loading Conditions, Procedia Eng. 74 (2014) 18–21.

[13] P. Lazzarin, R. Zambardi, A finite-volume-energy based approach to predict the static and fatigue behavior of components with sharp V-shaped notches, Int. J. Fracture 112 (2001) 275-98.

[14] F. Berto, P. Lazzarin, M.R. Ayatollahi, Brittle fracture of sharp and blunt V-notches in isostatic graphite under torsion loading, Carbon 50 (2012) 1942-52.

[15] P. Lazzarin, F. Berto, Some Expressions for the Strain Energy in a Finite Volume Surrounding the Root of Blunt V-notches, Int. J. Fracture 135 (2005) 161-85.

[16] P. Lazzarin, A. Campagnolo, F. Berto, A comparison among some recent energy- and stress-based criteria for the fracture assessment of sharp V-notched components under Mode I loading, Theor. Appl. Fract. Mec. 71 (2014) 21-30.

[17] P. Livieri, P. Lazzarin, Fatigue strength of steel and aluminium welded joints based on generalised stress intensity factors and local strain energy values, Int. J. Fracture 133 (2005) 247-76.

[18] F. Berto, M.R. Ayatollahi, T. Borsato, P. Ferro, Local strain energy density to predict size-dependent brittle fracture of cracked specimens under mixed mode loading, *Theor. Appl. Fract. Mech.* 86(B) (2016) 217-224.

[19] A.R. Torabi, F. Berto, S.M.J. Razavi, Ductile failure prediction of thin notched aluminum plates subjected to combined tension-shear loading. *Theor. Appl. Fract. Mech*. (in press). (DOI: 10.1016/j.tafmec.2017.05.003)

[20] A.R. Torabi, H.R. Majidi, M.R. Ayatollahi, Brittle failure of key-hole notches under mixed mode I/II loading with negative mode I condition, *Eng. Fract. Mech*. 168 (2016) 51-72.

[21] A. Torabi, F. Berto, S.M.J. Razavi, Tensile failure prediction of U-notched plates under moderate-scale and large-scale yielding regimes, *Theor. Appl. Fract. Mech*. (in press).

[22] P. Ferro, M. Zappalorto, The strain energy density approach applied to cyclic and transient thermo-mechanical problems. Proceedings of 4th Internationa Conference of Engineering against Failure (ICEAF) 24-26 June 2015 Skiathos Greece.

[23] P. Ferro, F. Berto, T. Borsato, Thermal load-induced notch stress intensity factor derived from averaged strain density. 21st European Conference on Fracture, ECF21, 20-24 June 2016. *Procedia Structural Integrity* (2016) Vol. 2, 2367-2374

[24] P. Ferro, The local strain energy density approach applied to pre-stressed components subjected to cyclic load, *Fatigue Fract. Eng. Mater. Struct. 37(11)* (2014) 1268-1280.

[25] P. Ferro, F. Berto, Quantification of the influence of residual stresses on fatigue strength of Al-alloy welded joints by means of the local strain density approach, *Strength Mater. 48(3)* (2016) 426–436.

[26] P. Ferro, F. Berto, N.M. James, Asymptotic residual stresses in butt-welded joints under fatigue loading, *Theor. Appl. Fract. Mech.* 83 (2016) 114–124.

[27] P. Ferro, F. Berto, M.N. James, T. Borsato, Review of recent advances in local approaches applied to pre-stressed components under fatigue loading, *Procedia Struct. Integrity* 2 (2016) 3467–3474

[28] S. Filippi, P. Lazzarin, R. Tovo, Developments of some explicit formulas useful to describe elastic stress fields ahead of notches in plates, *Int. J. Solids Struct*. 39 (2002) 4543–4565.

[29] M. Blattmeier, G. Witt, J. Wortberg, J. Eggert, J. Toepker, Influence of surface characteristics on fatigue behaviour of laser sintered plastics, *Rapid Prototyping J*. 18 (2) (2012) 161 - 171.

[30] J. Vaithilingam, R. D. Goodridge, S. D. Christie, S. Edmondson, R. J. M. Hague, Surface modification of selective laser melted structures using self - assembled monolayers for biomedical applications. Polishing. Solid Freeform Fabrication Symposium, Austin, TX, 2012.

[31] I. Yadroitsev, I. Smurov, Surface morphology in selective laser melting of metal powders, *Phys. Procedia* 12 (2011) 264 - 270.

[32] L. Yang, H. Gu, A. Lassell, Surface treatment of Ti6al4V parts made by powder bed fusion additive manufacturing processes using electropolishing, Proceedings of Solid Freeform Fabrication (SFF) Symposium, Austin, TX, 2014.

[33] F. Berto, A. Kotousov, P. Lazzarin, L.P. Pook, On scale effect in plates weakened by rounded V-notches and subjected to in-plane shear loading, *Int. J . Fract*. 180 (2013) 111-118.

[34] L.P. Pook, A. Campagnolo, F. Berto, P. Lazzarin, Coupled fracture mode of a cracked plate under anti-plane loading, *Eng. Fract. Mech*. 134 (2015) 391-403.

[35] F. Berto, P. Lazzarin, A. Kotousov, L.P. Pook, Induced out ‐ of ‐ plane mode at the tip of blunt lateral notches and holes under in ‐ plane shear loading, *Fatigue Fract. Eng. Mater. Struct*. 35 (2012) 538-555.

[36] S. Hosseini, Fatigue of Ti-6Al-4V, in: R. Hudak, M. Penhaker, J. Majernik (Eds.), Biomedical Engineering - Technical Applications in Medicine, 2012, ISBN 978-953-51-0733-0.

Table captions

Table 1. Parameters for the stress distribution [28].

Figure captions

Fig. 1. Coordinate system and symbols used for the stress field components ($q = \frac{2\pi - 2\alpha}{\pi}$, $\rho = \frac{qr_o}{q-1}$).

Fig. 2. Critical volume (area) for blunt V-notch under mode I loading condition.

Fig. 3. Geometries of smooth and blunt V-notched specimens and built axis (Z) (dimensions in mm).

Fig. 4. Fatigue life of smooth samples.

Fig. 5. Fatigue life of double blunt V-nothced samples.

Fig. 6. OM (a) and ESEM (b) micrographs of the sample in xy plane.

Fig. 7. ESEM fractographs of the smooth specimen ($\Delta\sigma$ = 320 MPa, Cycles Number = 410225).

Fig. 8. ESEM fractographs of the double blunt V-notched specimen ($\Delta\sigma$ = 220 MPa, Cycles Number = 156035).

Fig. 9. Numerical value of $\Delta\bar{W}_c^{bluntV-notch}$ as a function of the critical radius, R_c.

Fig. 10. Schematic representation of PSB formed in a crystal grain that has an unfavourable orientation of its (0001) slip planes relative to the planes of maximum applied shear stresses.

Fig. 11. Surface intrusions induced by the SLM process.

Table 1. Parameters for the stress distribution [28].

2α (rad)	q	λ_1	μ_1	χ_{b1}	χ_{c1}	χ_{d1}
0	2.0000	0.5000	-0.5000	1	4	0
$\pi/6$	1.8333	0.5014	-0.4561	1.0707	3.7907	0.0632
$\pi/4$	1.7500	0.5050	-0.4319	1.1656	3.5721	0.0828
$\pi/3$	1.6667	0.5122	-0.4057	1.3123	3.2832	0.0960
$\pi/2$	1.5000	0.5448	-0.3449	1.8414	2.5057	0.1046
$2\pi/3$	1.3334	0.6157	-0.2678	3.0027	1.5150	0.0871
$3\pi/4$	1.2500	0.6736	-0.2198	4.1530	0.9933	0.0673
$5\pi/6$	1.1667	0.7520	-0.1624	6.3617	0.5137	0.0413

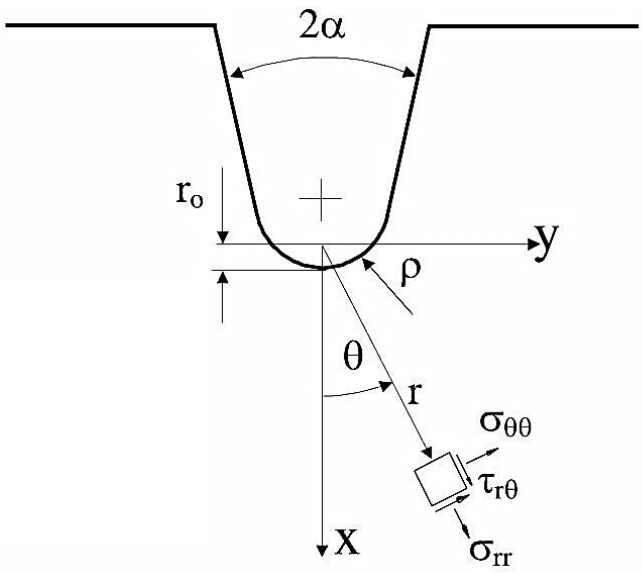

Fig. 1. Coordinate system and symbols used for the stress field components ($q = \frac{2\pi - 2\alpha}{\pi}$, $\rho = \frac{qr_o}{q-1}$).

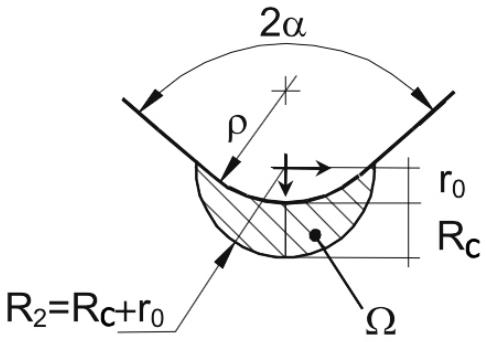

Fig. 2. Critical volume (area) for blunt V-notch under mode I loading condition.

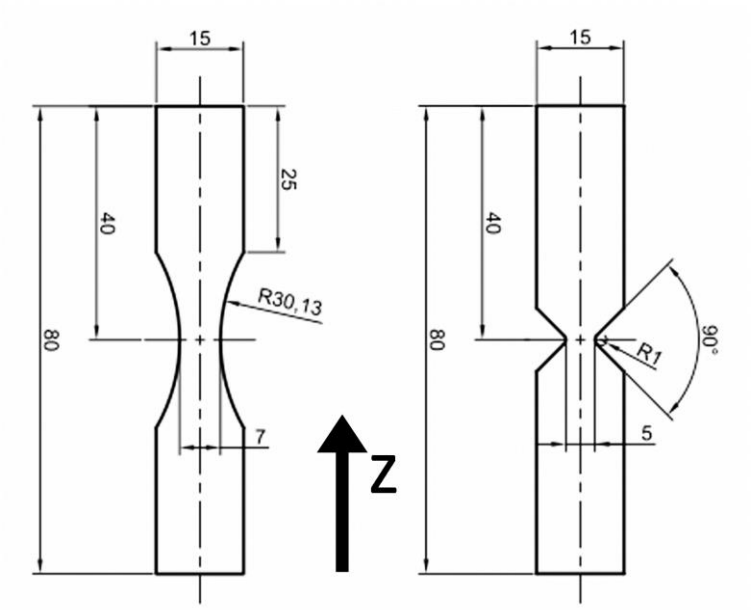

Fig. 3. Geometries of smooth and blunt V-notched specimens and built axis (Z) (dimensions in mm).

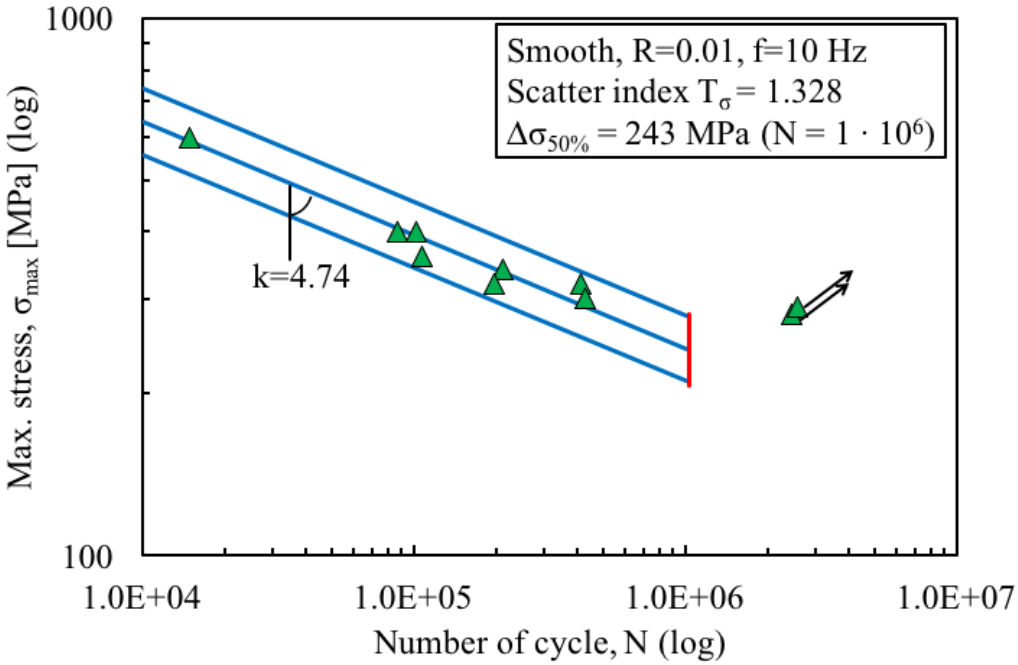

Fig. 4. Fatigue life of smooth samples.

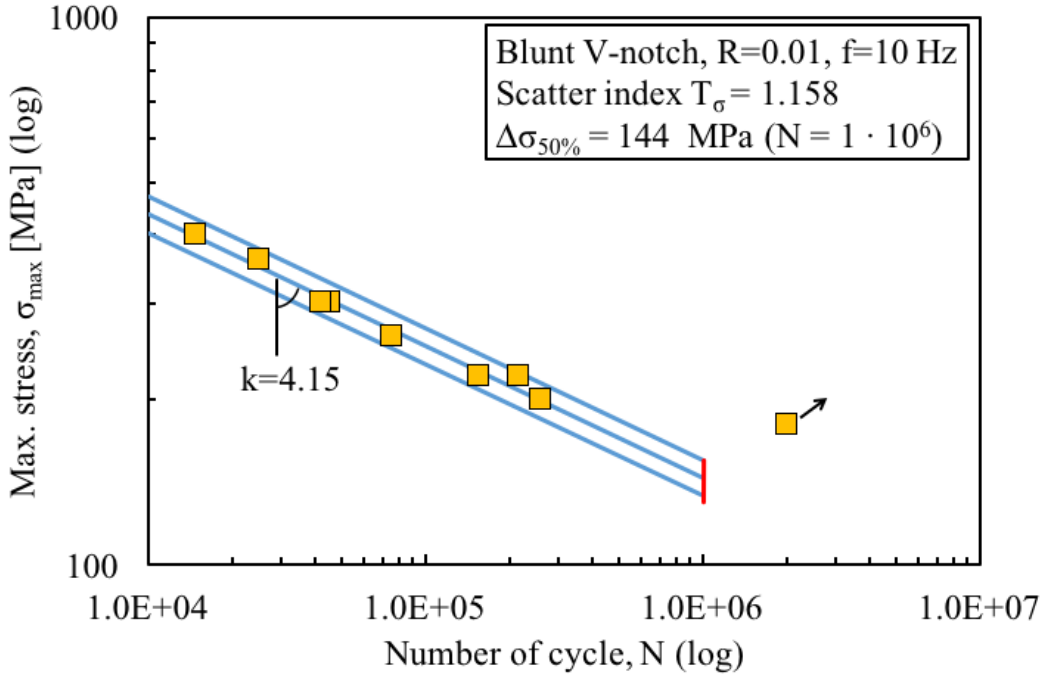

Fig. 5. Fatigue life of double blunt V-nothced samples.

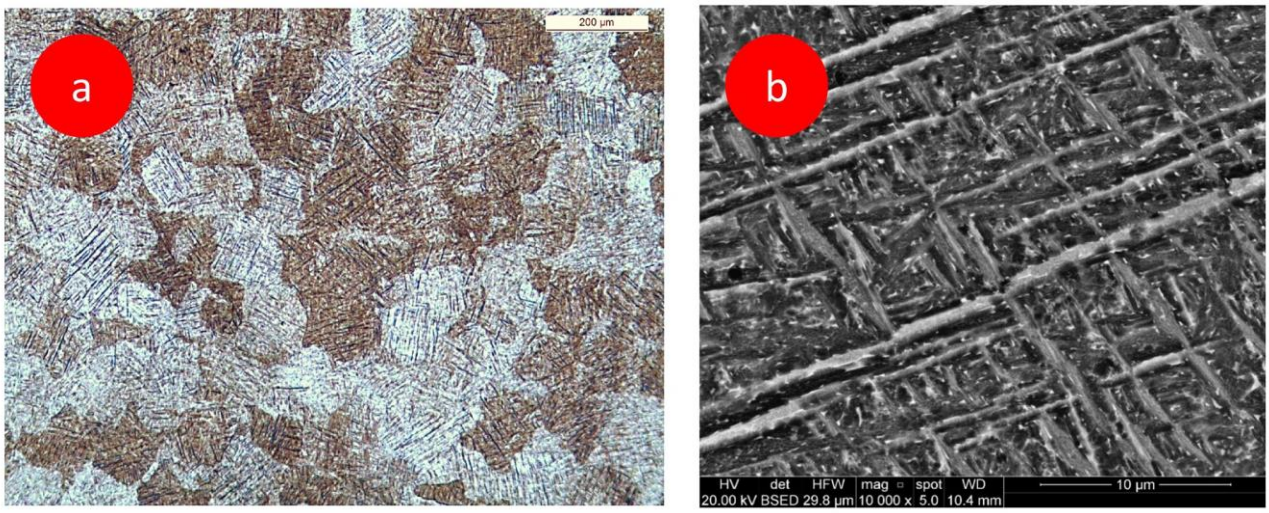

Fig. 6. OM (a) and ESEM (b) micrographs of the sample in xy plane.

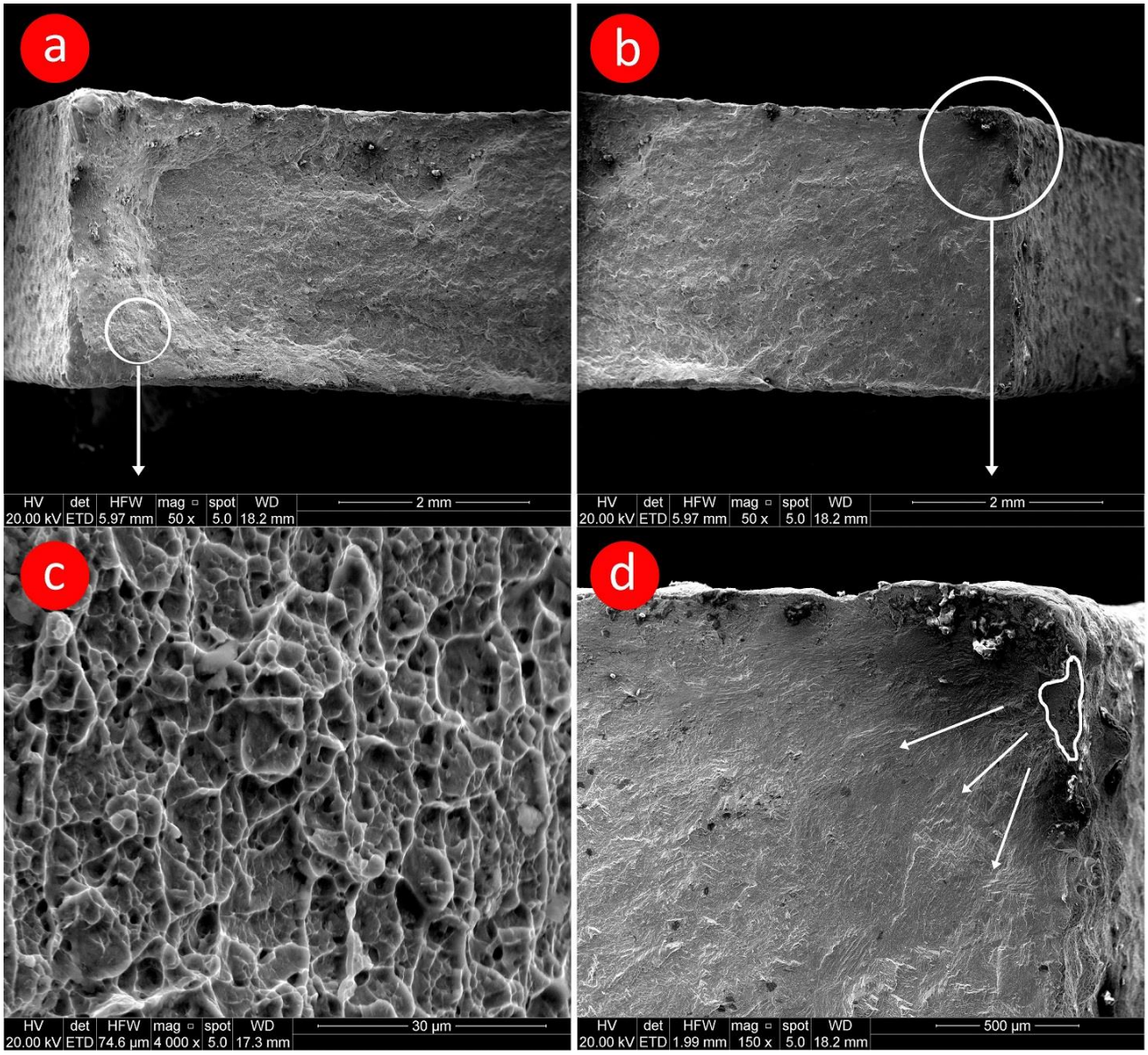

Fig. 7. ESEM fractographs of the smooth specimen ($\Delta\sigma$ = 320 MPa, Cycles Number = 410225).

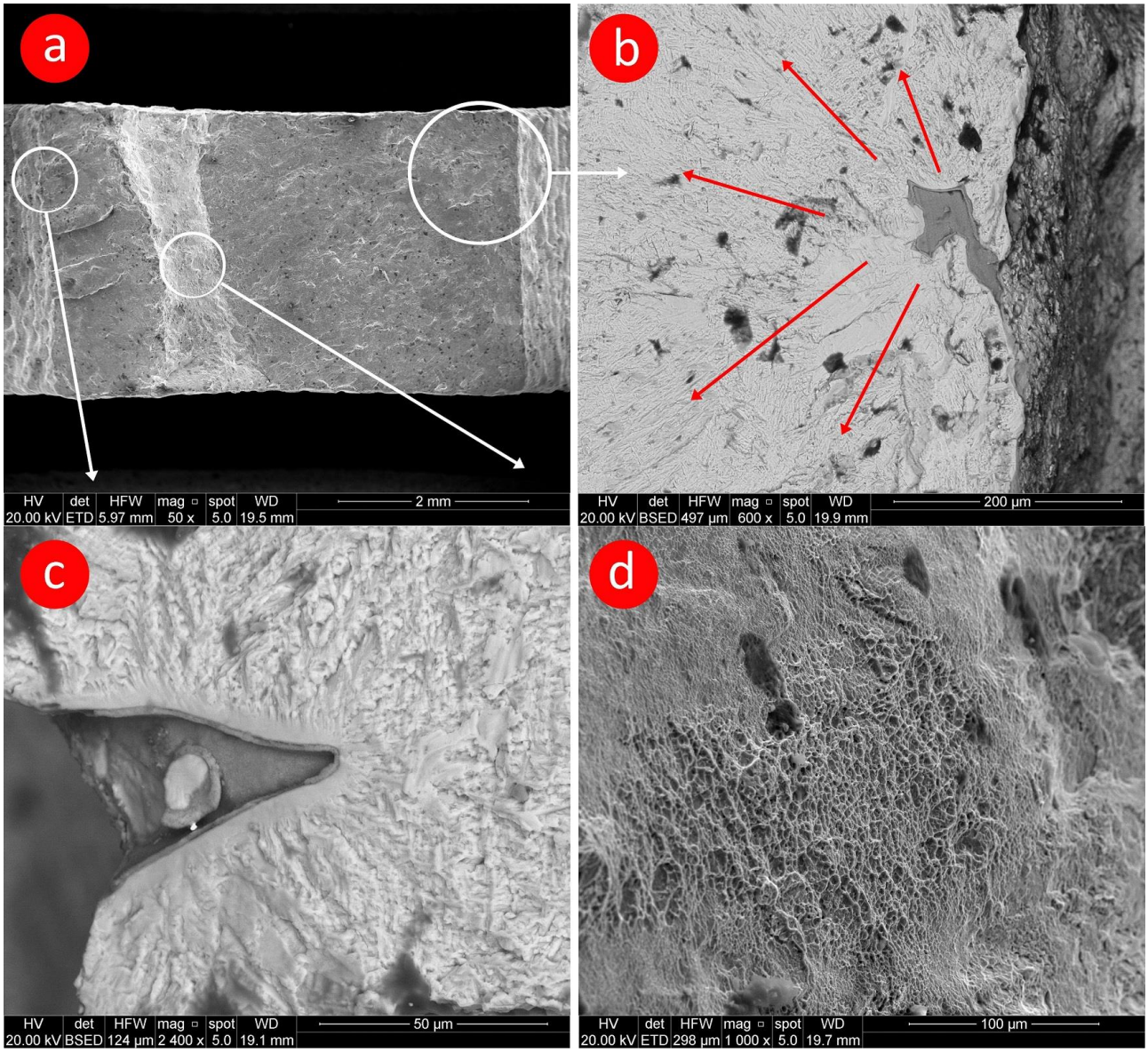

Fig. 8. ESEM fractographs of the double blunt V-notched specimen ($\Delta\sigma$ = 220 MPa, Cycles Number = 156035).

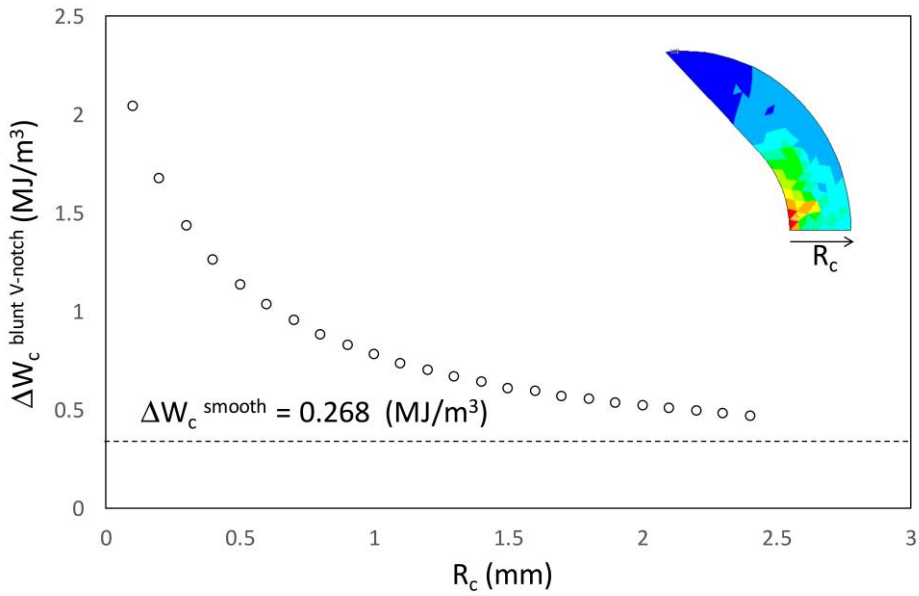

Fig. 9. Numerical value of $\Delta \overline{W}_c^{bluntV-notch}$ as a function of the critical radius, R_c.

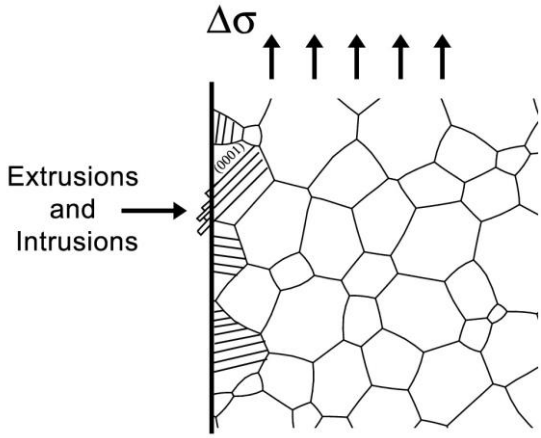

Fig. 10. Schematic representation of PSB formed in a crystal grain that has an unfavourable orientation of its (0001) slip planes relative to the planes of maximum applied shear stresses.

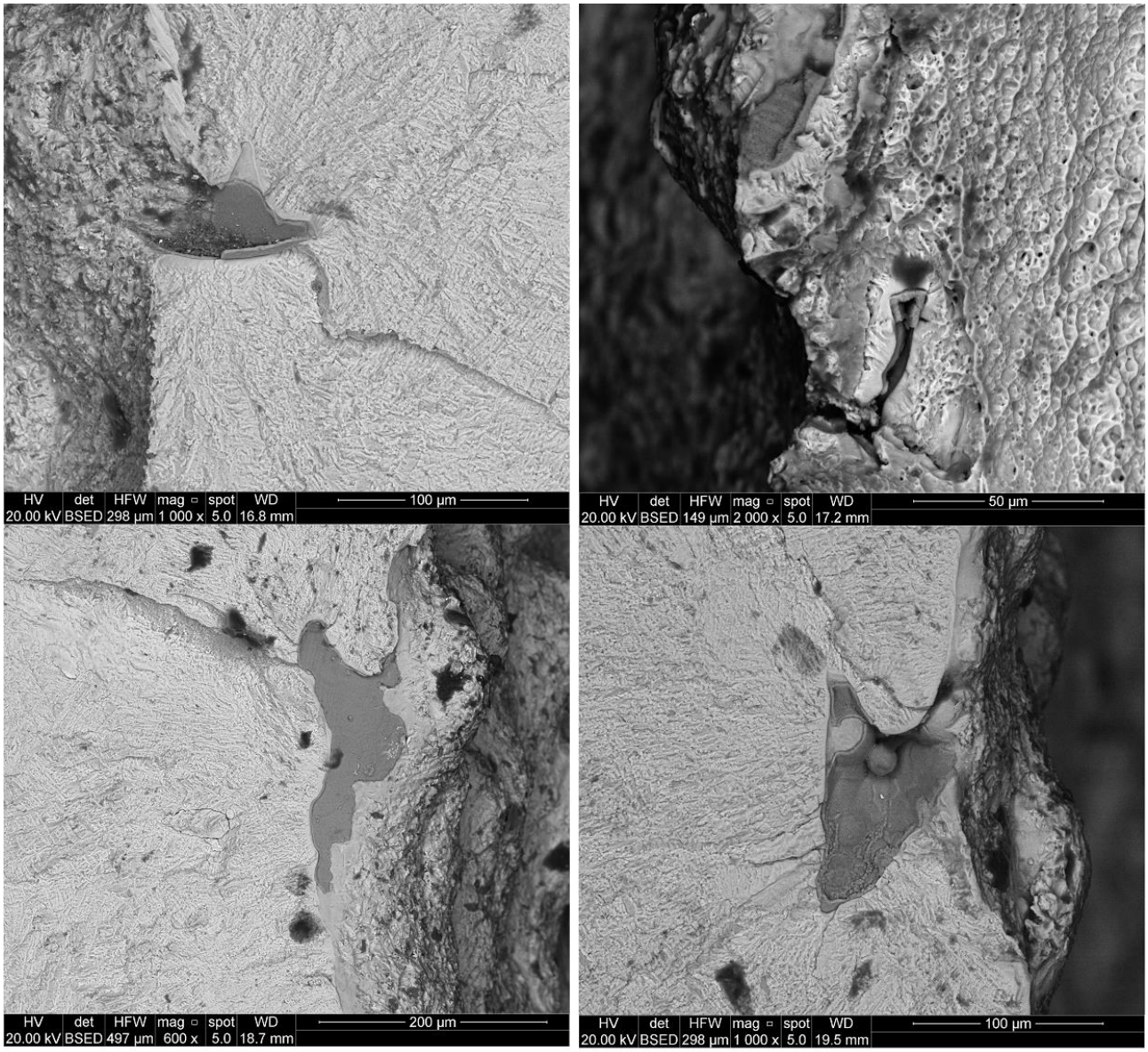

Fig. 11. Surface intrusions induced by the SLM process.